

# Visualization of electronic topology in ZrSiSe by scanning tunneling microscopy

Kunliang Bu,<sup>1</sup> Ying Fei,<sup>1</sup> Wenhao Zhang,<sup>1</sup> Yuan Zheng,<sup>1</sup> Jianlan Wu,<sup>1</sup> Fangchu Chen,<sup>2,3</sup> Xuan Luo,<sup>2</sup> Yuping Sun,<sup>2,4,5</sup> Qiunan Xu,<sup>6</sup> Xi Dai,<sup>6,7</sup> and Yi Yin<sup>1,5,\*</sup>

<sup>1</sup>*Department of Physics, Zhejiang University, Hangzhou 310027, China*

<sup>2</sup>*Key Laboratory of Materials Physics, Institute of Solid State Physics, Chinese Academy of Sciences, Hefei 230031, China*

<sup>3</sup>*University of Science and Technology of China, Hefei 230026, China*

<sup>4</sup>*High Magnetic Field Laboratory, Chinese Academy of Sciences, Hefei 230031, China*

<sup>5</sup>*Collaborative Innovation Center of Advanced Microstructures, Nanjing 210093, China*

<sup>6</sup>*Beijing National Laboratory for Condensed Matter Physics and Institute of Physics, Chinese Academy of Sciences, Beijing 100190, China*

<sup>7</sup>*Department of Physics, Hong Kong University of Science and Technology, Clear Water Bay Road, Kowloon, Hong Kong*

## Abstract

As emerging topological nodal-line semimetals, the family of ZrSiX ( $X = \text{O}, \text{S}, \text{Se}, \text{Te}$ ) has attracted broad interests in condensed matter physics due to their future applications in spintronics. Here, we apply a scanning tunneling microscopy (STM) to study the structural symmetry and electronic topology of ZrSiSe. The glide mirror symmetry is verified by quantifying the lattice structure of the ZrSe bilayer based on bias selective topographies. The quasiparticle interference analysis is used to identify the band structure of ZrSiSe. The nodal line is experimentally determined at  $\sim 250$  meV above the Fermi level. An extra surface state Dirac point at  $\sim 400$  meV below the Fermi level is also determined. Our STM measurement provides a direct experimental evidence of the nodal-line state in the family of ZrSiX.

The topology of electronic bands is closely correlated with intrinsic symmetries in topological materials [1]. The three dimensional (3D) Dirac semimetals host a fourfold degenerate Dirac point, which is protected by spatial inversion symmetry, time reversal symmetry and additional threefold or fourfold rotational symmetry along the  $z$ -axis [2, 3]. If one symmetry is broken, the spin-doublet degeneracy of the bands is removed and the Dirac point is changed to the twofold degenerate Weyl point, leading to a Weyl semimetal [4–7]. In contrast, the topological nodal-line semimetals host a loop of Dirac points in the momentum space, which has recently been predicted theoretically and verified experimentally [8–10]. The formation of a nodal line requires extra symmetries, such as mirror reflection symmetry [8] or glide mirror symmetry [9]. The appearance of Dirac or Weyl points near the Fermi level gives rise to exotic electronic properties, such as large magnetoresistance [11–14], high carrier density [15] and mobility [11, 12, 16]. The nodal-line semimetals are thus good candidates of spintronics for both fundamental research and future applications.

In a previous study, a nodal line was observed in the band structure of  $\text{PaTaSe}_2$  [8]. Due to interference of other bands, the investigation of nodal-line Dirac fermions is difficult around the Fermi level. In a different family of  $\text{ZrSiX}$  ( $X = \text{O}, \text{S}, \text{Se}, \text{Te}$ ) semimetals with glide mirror symmetry, the nodal line is theoretically predicted [9]. The calculation shows that the Dirac cone is linearly dispersed in a large energy range ( $\sim 2$  eV), without interference of other bands. Through the measurement of the band structure below the Fermi level, angle-resolved photoemission spectroscopy (ARPES) has probed the linear band dispersions of  $\text{ZrSiS}$  and  $\text{ZrSiSe}$  [17–19]. However, the theoretical prediction of the nodal line is above the Fermi level so that ARPES cannot make a direct measurement. Instead, scanning tunneling microscope (STM) is a powerful tool to detect both the topography and local density of states (LDOS), which provides a transparent view of microscopic properties. A quasiparticle interference (QPI) technique can be used to extract the band structure in a broad energy above and below the Fermi level [20]. The previous STM measurements on  $\text{ZrSiS}$  however did not really determine the nodal-line state due to their limitations in data acquisition and analysis [21, 22].

In this paper, we take the STM measurement on  $\text{ZrSiSe}$ . Our study resolves a bias selective topography and precisely identifies an atomic shift between Zr and Se sublattices, giving an evidence of the glide mirror symmetry in  $\text{ZrSiSe}$ . The QPI analysis visualizes the linear band dispersion, which determines a nodal line located at  $\sim 250$  meV above the Fermi

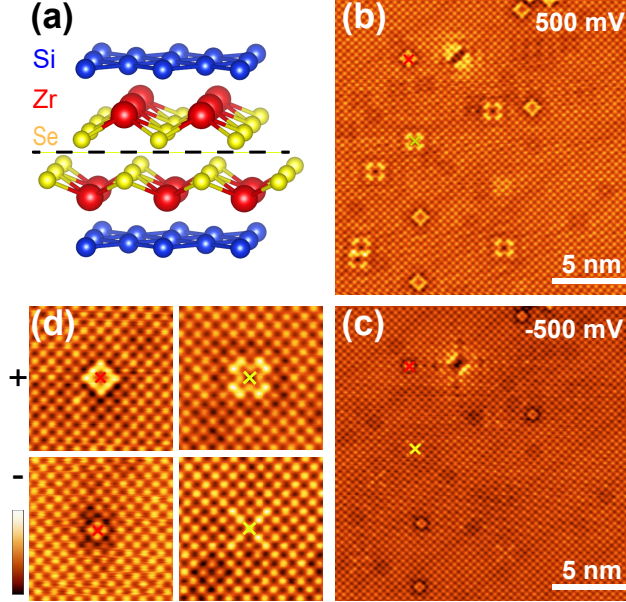


FIG. 1. (a) A schematic diagram of ZrSiSe. Two  $20 \text{ nm} \times 20 \text{ nm}$  topographic images of the same FOV under the tunneling current of  $I = 400 \text{ pA}$  and the bias voltages of (b)  $V_b = 500 \text{ mV}$  and (c)  $V_b = -500 \text{ mV}$ . The local topographic images of two defects labelled by the red and yellow crosses are enlarged in (d), where the upper and lower panels correspond to the positive and negative bias voltages, respectively.

level and a Dirac point located at  $\sim 400 \text{ meV}$  below the Fermi level. Our measurement is thus the first STM determination of the nodal-line state in the family of ZrSiX.

High-quality single crystals of ZrSiSe in our experiment are grown by the chemical vapor transport method. STM measurements are carried out in a commercial ultra-high vacuum system [23]. The samples are cleaved *in situ* at liquid nitrogen temperature and immediately inserted into the STM head. An electrochemically etched tungsten tip is treated with the field emission on a single crystalline of Au(111) surface. All data are acquired at liquid helium temperature ( $\sim 4.5 \text{ K}$ ).

The crystal structure of ZrSiSe is in the space group of  $P4/nmm$  [9]. As shown in Fig. 1(a), each Si square layer is sandwiched by two sets of ZrSe bilayers. The crystal is cleaved in between two adjacent ZrSe bilayers and a Se square layer is exposed to be the surface plane. Figures 1(b) and 1(c) display topographies under two opposite bias voltages in the same field of view (FOV). The detected lattice is shifted from the top to hollow sites when the bias voltage is switched. As an illustration, we present enlarged images of two

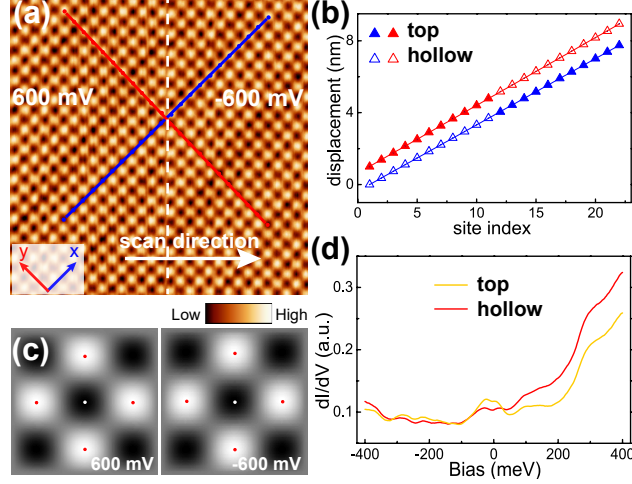


FIG. 2. (a) A  $8 \text{ nm} \times 8 \text{ nm}$  topographic image where the bias voltage is switched from  $V_b = 600 \text{ mV}$  to  $V_b = -600 \text{ mV}$  when crossing the dashed line. (b) The relative displacement of each site (top or hollow) along the blue and red linecuts in (a). Data are offset vertically for clarity. The up-triangles represent the experimental result and the solid lines are from a linear fitting. The solid and open up-triangles refer to the top and hollow sites, respectively. (c) The two ‘supercell’ images obtained for the left and right topographic images in (a). The bright and dark spots refer to the averaged top and hollow sites, with red and white dots labeling their centers. (d) The average  $dI/dV$  spectra at the top (orange) and hollow (red) sites under the negative bias voltage.

defects in Fig. 1(d). Under the positive bias voltage [Fig. 1(d), upper panels], the centers of the diamond and cross shaped defects are at the top and hollow sites, respectively. Under the negative bias voltage [Fig. 1(d), lower panels], these two centers are switched to their opposite sites. Two different sublattices are detected in the STM, each selected by a specific bias voltage polarity.

To further explore the atomic structure of ZrSiSe, we perform a designed experiment on a clean surface. As shown in Fig. 2(a), the topography is scanned along the left-to-right direction. The applied bias voltage is initially positive and suddenly switched to a negative value at an intermediate position [Fig. 2(a), dashed line]. With respect to this switching line, the left and right topographies are shifted due to the change of the bias voltage. Two linecuts (blue and red) along the  $x$ - and  $y$ -directions are selected as a demonstration. The red line crosses the top sites under the positive bias and then the hollow sites under the negative bias. In Fig. 2(b), we record the sequence of these sites and plot their relative

displacements, which are in a perfect linear relation with the site index. The same behavior is observed for the sites along the blue line. The hollow sites under the negative bias are thus extended from the top sites under the positive bias, and vice versa.

For each of the left and right topographies, a ‘supercell’ technique [24–26] is applied to extract an averaged image with a significantly reduced error. The  $(\pm a_0/2, \pm a_0/2)$  spatial displacement with the lattice constant  $a_0 = 3.62 \text{ \AA}$  is precisely determined between neighboring top and hollow sites for both topographies [Fig. 2(c)]. Under a given bias voltage, the top and hollow sites form two different sublattices, attributed to two planes of the ZrSe bilayer. To identify their components, we average the  $dI/dV$  spectra over the top and hollow sites separately. The local density of unoccupied states at the hollow sites is consistently larger than that at the top sites [Fig. 2(d)]. The  $5d$  orbitals of Zr atoms are highly unoccupied while the  $4p$  orbitals of Se atoms are highly filled. Thus, the sublattices of the top and hollow sites with the negative bias correspond to the Se and Zr layers, respectively. The opposite result can be obtained for the positive bias. Our topography measurement visualizes the atomically resolved structure of the ZrSe bilayer, which obeys a key requirement of the glide mirror symmetry in ZrSiSe.

The Fourier transformed scanning tunneling spectroscopy (FT-STs) is next employed to detect the electronic topology of ZrSiSe, which is resulted directly from its structural symmetry. With a bias voltage of 500 mV, the topography of a new FOV is displayed in Fig. 3(a), in which a specific cross-shaped impurity is found on the top right corner. The  $dI/dV$  conductance map simultaneously taken under the same bias voltage is drawn in Fig. 3(b). This specific cross-shaped impurity induces a strong elastic scattering, which mixes the electronic eigenstates of different wavevectors ( $\mathbf{k}_i$  and  $\mathbf{k}_f$ ) but the same energy. The QPI is signalled by a standing wave in the LDOS around the impurity, as shown by an enlarged image in the inset of Fig. 3(b). The Fourier transform of this local conductance map is drawn in Fig. 3(d). The QPI patterns in the momentum  $\mathbf{q}$ -space can be used to identify the wavevector difference before and after the elastic scattering ( $\mathbf{q} = \mathbf{k}_f - \mathbf{k}_i$ ), which helps building the contour of constant energy (CCE). As shown in Fig. 3(d), the centrally symmetric QPI patterns can be mainly partitioned into three groups: a diamond, two concentric squares, and four sets of triplet lines. For these pattern groups, we assign their typical scattering wavevectors, labelled from  $\mathbf{q}_1$  to  $\mathbf{q}_4$  in different colors. Other QPI patterns cannot be ruled out due to the resolution of our FT-STs map. In addition, the

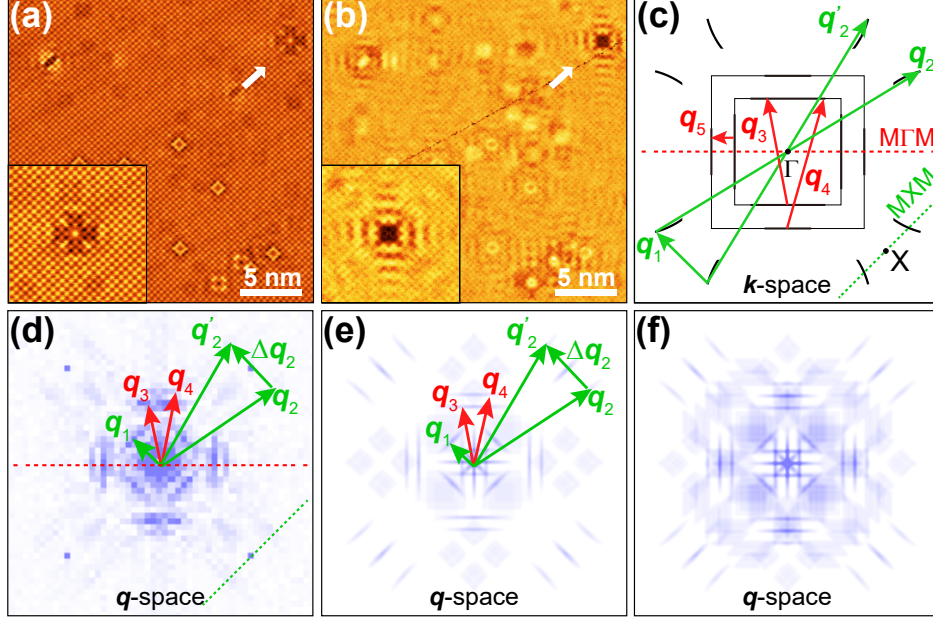


FIG. 3. (a) A  $25 \text{ nm} \times 25 \text{ nm}$  topographic image with bias voltage  $V_b = 500 \text{ mV}$ . (b) The  $dI/dV$  conductance map at  $V = 500 \text{ mV}$  simultaneously taken with (a). The insets of (a) and (b) show the enlarged images around a cross-shaped impurity labelled by a white arrow. (c) A CCE model in the momentum  $\mathbf{k}$ -space. (d) The experimental QPI map in the momentum  $\mathbf{q}$ -space using Fourier transform of the local conductance map in the inset of (b). (e) and (f) are the calculated QPI maps using the CCE model with and without a selection rule (see text). The typical scattering wavevectors responsible for the major QPI patterns are shown in (c)-(e).

structure of QPI patterns changes with the scattering impurity and more discussions are provided in Supplementary Materials.

To interpret the three groups of QPI patterns, we propose a model CCE with two groups of  $E(\mathbf{k})$  patterns in Fig. 3(c). The first group includes four pairs of short arcs around four X points, contributing to the diamond ( $\mathbf{q}_1$ ) and triplet ( $\mathbf{q}_2$  and  $\mathbf{q}'_2$ ) QPI patterns. The diamond pattern results from scattering between the arcs of the same pair, while the triplet pattern results from scattering between the arcs at the diagonal corners. The second group consists of two concentric squares of  $E(\mathbf{k})$ , contributing to the concentric squares of the QPI patterns ( $\mathbf{q}_3$  and  $\mathbf{q}_4$ ). The two groups of CCE patterns are similar to those observed in ARPES [19]. However, a key difference is that only the occupied states below the Fermi level are detected in ARPES. To reproduce the experimental QPI patterns, we introduce a selection rule that the elastic scattering only occurs between the CCE patterns of the

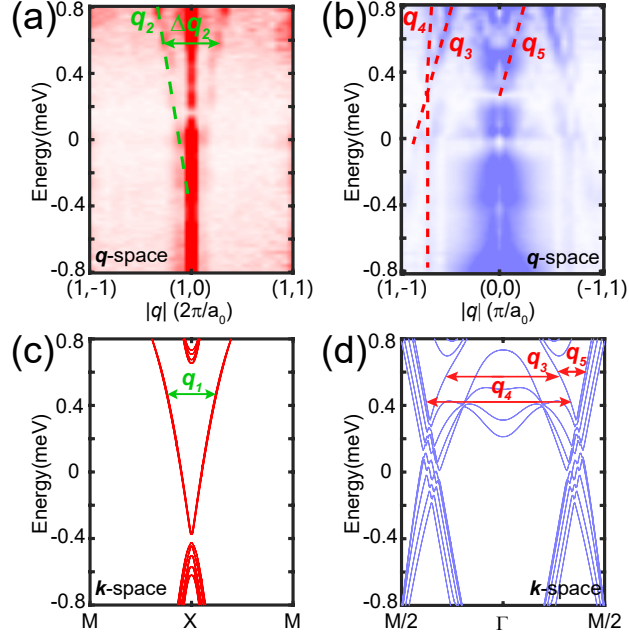


FIG. 4. (a) and (b) present the QPI energy dispersions along the green and red dashed lines in the  $\mathbf{q}$ -space [Fig. 3(d)]. The energy dispersions of the wavevectors relevant to the electronic topology are highlighted in dashed lines in (a) and (b). (c) and (d) present the DFT calculation of the slab band structure along the M-X-M and M- $\Gamma$ -M directions in the  $\mathbf{k}$ -space.

same group. The physical mechanism behind this selection rule is that the two CCE groups belong to the surface and bulk bands separately [17]. The QPI map calculated based on the CCE model and the selection rule [Fig. 3(e)] shares the same major features as those from the experimental measurement [Fig. 3(d)]. As a comparison, the calculation without the selection rule [Fig. 3(f)] clearly deviates from the experimental result.

Next we measure the energy dependent conductance maps around this impurity and study the energy dispersion relations. Figure 4(a) presents the result of  $\mathbf{q}(E)$  along the green line in the  $\mathbf{q}$ -space [Fig. 3(d)]. The triplet QPI pattern [Fig. 3(d)] is gradually compressed as the energy approaches the Fermi level from above. A linear energy dispersion of the scattering wavevectors,  $\mathbf{q}_2$  and  $\mathbf{q}'_2$ , is observed. Their difference,  $\Delta\mathbf{q}_2 = \mathbf{q}'_2 - \mathbf{q}_2$ , vanishes roughly at the bias voltage of  $\sim -400$  mV, indicating a Dirac cone in the electronic band structure. Due to the scattering within the same CCE group, a simple relation,  $\Delta\mathbf{q}_2 = 2\mathbf{q}_1$ , holds. The energy dispersion of  $\mathbf{q}_1$  (not shown) follows the same behavior of  $\Delta\mathbf{q}_2$ , further confirming the existence of the Dirac cone. In Fig. 4(c), we provide the density functional theory

(DFT) calculation of the slab band structure along the M-X-M direction in the  $\mathbf{k}$ -space. The predicted Dirac point, if ignoring the small gap due to the spin-orbital coupling (SOC), is consistent with our experimental measurement. In addition, this Dirac cone is a surface derived state since it is not observed in the DFT calculation of the bulk ZrSiSe.

Figure 4(b) presents the result of  $\mathbf{q}(E)$  along the red line in the  $\mathbf{q}$ -space [Fig. 3(d)]. As the energy approaches the Fermi level from above, the sizes of the two concentric QPI squares [Fig. 3(d)] are both enlarged, but with different speeds. These two squares are merged into a single square, indicating the appearance of a nodal line. The linear energy dispersion is also found for the scattering wavevectors,  $\mathbf{q}_3$  and  $\mathbf{q}_4$ . As the amplitude of  $\mathbf{q}_3$  is increased faster than that of  $\mathbf{q}_4$ , the crossing point of these two wavevectors leads to an estimation of the nodal line at the energy of  $\sim 250$  meV above the Fermi level. In our CCE model,  $\mathbf{q}_3$  arises from the scattering within the inner square, while  $\mathbf{q}_4$  arises from the scattering between the two opposite sides of the inner and outer squares [Fig. 3(c)]. A possibility causing the change of the  $\mathbf{q}_3$  and  $\mathbf{q}_4$  is that the inner square is expanded and the outer square is shrunk with the decrease of energy. In Fig. 4(d), we present the DFT calculation of the slab band structure along the M- $\Gamma$ -M direction in the  $\mathbf{k}$ -space. The above conjecture of the dispersion relation of the two bands is confirmed theoretically. In addition to  $\mathbf{q}_3$  and  $\mathbf{q}_4$ , another scattering wavevector  $\mathbf{q}_5$  is also observed due to the scattering between the same sides of the inner and outer CCE squares [Fig. 3(c)]. The dispersion relation of  $\mathbf{q}_5$  [Fig. 4(b)] confirms the nodal line at the same energy level as that estimated from the merging of  $\mathbf{q}_3$  and  $\mathbf{q}_4$ . Compared to the surface derived Dirac point at the X point, this nodal line is attributed to the bulk band structure, as shown by the DFT calculation. An interesting phenomenon is that the QPI pattern due to the scattering within the outer CCE square is missing, which is possibly due to the impurity sensitivity on the band scattering.

In summary, we perform a sophisticated STM experiment on a novel 3D topological semimetal, ZrSiSe. The bias selective topographies allow us to identify the lattice structure of the ZrSe bilayer with a sub-atomic resolution, which confirms the glide mirror symmetry in ZrSiSe. The QPI technique in the FT-STs measurement is further applied to extract the electronic structure of ZrSiSe. By analyzing QPI patterns with assistance of the CCE model and DFT calculation, we determine the nodal line in the bulk band, at  $\sim 250$  meV above the Fermi level. In addition, a Dirac point is also determined at  $\sim 400$  meV below the Fermi level. Compared to an indirect determination in previous ARPES studies, our STM



measurement directly visualizes the topological nodal-line state in ZrSiSe. This method can be generalized to other nodal-line semimetals in the same family, including two dimensional films.

This work was supported by the National Basic Research Program of China (2014CB921203 and 2015CB921004), the National Natural Science Foundation of China (NSFC-11374260), and the Fundamental Research Funds for the Central Universities in China. F.C., X.L. and Y.S. thank the support of the National Key Research and Development Program (2016YFA0300404) and the National Nature Science Foundation of China (NSFC-11674326) and the Joint Funds of the National Natural Science Foundation of China and the Chinese Academy of Sciences' Large-Scale Scientific Facility (U1432139).

K.B. and Y.F. contribute equally to this work.

---

\* yiyin@zju.edu.cn

- [1] C.-K. Chiu, J. C. Y. Teo, A. P. Schnyder, and S. Ryu, *Rev. Mod. Phys.* **88**, 035005 (2016).
- [2] Z. J. Wang, Y. Sun, X.-Q. Chen, C. Franchini, G. Xu, H. M. Weng, X. Dai, and Z. Fang, *Phys. Rev. B* **85**, 195320 (2012).
- [3] Z. K. Liu, B. Zhou, Y. Zhang, Z. J. Wang, H. Weng, D. Prabhakaran, S.-K. Mo, Z.-X. Shen, Z. Fang, X. Dai, Z. Hussain, and Y. L. Chen, *Science* **343**, 864 (2014).
- [4] H. M. Weng, C. Fang, Z. Fang, B. A. Bernevig, and X. Dai, *Phys. Rev. X* **5**, 011029 (2015).
- [5] B. Q. Lv, H. M. Weng, B. B. Fu, X. P. Wang, H. Miao, J. Ma, P. Richard, X. C. Huang, L. X. Zhao, G. F. Chen, Z. Fang, X. Dai, T. Qian, and H. Ding, *Phys. Rev. X* **5**, 031013 (2015).
- [6] S.-Y. Xu, I. Belopolski, N. Alidoust, M. Neupane, G. Bian, C.L. Zhang, R. Sankar, G. Q. Chang, Z. J. Yuan, C.-C. Lee, S.-M. Huang, H. Zheng, J. Ma, D. S. Sanchez, B. K. Wang, A. Bansil, F. C. Chou, P. P. Shibayev, H. Lin, S. Jia, and M. Z. Hasan, *Science* **349**, 613–617 (2015).
- [7] H. Inoue, A. Gyenis, Z. J. Wang, J. Li, S. W. Oh, S. Jiang, N. Ni, B. A. Bernevig, and A. Yazdani, *AAAS* **351**, 1184–1187 (2016).
- [8] G. Bian, T.-R. Chang, R. Sankar, S.-Y. Xu, H. Zheng, T. Neupert, C.-K. Chiu, S.-M. Huang, G. Chang, I. Belopolski, D. S. Sanchez, M. Neupane, C. Liu, B. Wang, C.-C. Lee, H.-T. Jeng, C. Zhang, Z. Yuan, S. Jia, A. Bansil, F. Chou, H. Lin, and M. Z. Hasan, *Nat. Commun.* **7**,

- 10556 (2016).
- [9] Q. Xu, Z. Song, S. Nie, H. Weng, Z. Fang, and X. Dai, *Phys. Rev. B* **92**, 205310 (2015).
  - [10] J. Hu, Z. J. Tang, J. Y. Liu, X. Liu, Y. L. Zhu, D. Graf, K. Myhro, S. Tran, C. N. Lau, J. Wei, and Z. Q. Mao, *Phys. Rev. Lett.* **117**, 016602 (2016).
  - [11] M. N. Ali, L. M. Schoop, C. Garg, J. M. Lippmann, R. Lara, B. Lotsch, and S. S. P. Parkin, *Sci. Adv.* **2**, e1601742 (2016).
  - [12] X. F. Wang, X. C. Pan, M. Gao, J. H. Yu, J. Jiang, J. R. Zhang, H. K. Zuo, M. H. Zhang, Z. X. Wei, W. Niu, Z. C. Xia, X. G. Wan, Y. L. Chen, F. Q. Song, Y. B. Xu, B. G. Wang, G. H. Wang, and R. Zhang, *Adv. Electron. Mater.* **2**, (2016).
  - [13] Y.-Y. Lv, B.-B. Zhang, X. Li, S.-H. Yao, Y. B. Chen, J. Zhou, S.-T. Zhang, M.-H. Lu, and Y.-F. Chen, *Appl. Phys. Lett.* **108**, 244101 (2016).
  - [14] R. Singha, A. K. Pariari, B. Satpati, and P. Mandal, *Proc. Natl. Acad. Sci.* **114**, 2468 (2017).
  - [15] J. Hu, Z. J. Tang, J. Y. Liu, Y. L. Zhu, J. Wei, and Z. Q. Mao, *Phys. Rev. B* **96**, 045127 (2017).
  - [16] R. Sankar, G. Peramaiyan, I. P. Muthuselvam, C. J. Butler, K. Dimitri, M. Neupane, G. N. Rao, M.-T. Lin, and F. C. Chou, *Sci. Rep.* **7**, 40603 (2017).
  - [17] L. M. Schoop, M. N. Ali, C. Straßer, A. Topp, A. Varykhalov, D. Marchenko, V. Duppel, S. S. P. Stuart, B. V. Lotsch, and C. R. Ast, *Nat. Commun.* **7**, (2016).
  - [18] M. Neupane, I. Belopolski, M. M. Hosen, D. S. Sanchez, R. Sankar, M. Szlawska, S.-Y. Xu, K. Dimitri, N. Dhakal, P. Maldonado, P. M. Oppeneer, D. Kaczorowski, F.-C. Chou, M. Z. Hasan, and T. Durakiewicz, *Phys. Rev. B* **93**, 201104 (2016).
  - [19] M. M. Hosen, K. Dimitri, I. Belopolski, P. Maldonado, R. Sankar, N. Dhakal, G. Dhakal, T. Cole, P. M. Oppeneer, D. Kaczorowski, F.-C. Chou, M. Z. Hasan, T. Durakiewicz, and M. Neupane, *Phys. Rev. B* **95**, 161101 (2017).
  - [20] J. E. Hoffman, K. McElroy, D.-H. Lee, K. M. Lang, H. Eisaki, S. Uchida, and J. C. Davis, *Science* **297**, 1148 (2002).
  - [21] C. J. Butler, Y.-M. Wu, C.-R. Hsing, Y. Tseng, R. Sankar, C.-M. Wei, F.-C. Chou, and M.-T. Lin, *Phys. Rev. B* **96**, 195125 (2017).
  - [22] M. S. Lodge, G. Chang, C. Y. Huang, B. Singh, J. Hellerstedt, M. T. Edmonds, D. Kaczorowski, M. M. Hosen, M. Neupane, H. Lin, M. S. Fuhrer, B. Weber, and M. Ishigami, *Nano. Lett.* **17**, 7213 (2017).

- [23] Y. Zheng, Y. Fei, K. L. Bu, W. H. Zhang, Y. Ding, X. J. Zhou, J. E. Hoffman, and Y. Yin, *Sci. Rep.* **7**, 8059 (2017).
- [24] M. J. Lawler, K. Fujita, J. Lee, A. R. Schmidt, Y. Kohsaka, C. K. Kim, H. Eisaki, S. Uchida, J. C. Davis, J. P. Sethna, and E.-A. Kim, *Nature* **466**, 347 (2010).
- [25] K. Fujita, C. K. Kim, I. Lee, J. Lee, M. H. Hamidian, I. A. Firmo, S. Mukhopadhyay, H. Eisaki, S. Uchida, M. J. Lawler, E.-A. Kim, and J. C. Davis, *Science* **344**, 612 (2014).
- [26] I. Zeljkovic, Y. Okada, M. Serbyn, R. Sankar, W. Raman, D. Walkup, W. Zhou, J. Liu, G. Chang, Y. J. Wang, M. Z. Hasan, F. C. Chou, H. Lin, A. Bansil, L. Fu, and V. Madhavan, *Nat. Mater.* **14**, 318 (2015).

**Supplemental Material for**  
**“Visualization of electronic topology in ZrSiSe by**  
**scanning tunneling microscopy”**

Kunliang Bu,<sup>1</sup> Ying Fei,<sup>1</sup> Wenhao Zhang,<sup>1</sup> Yuan Zheng,<sup>1</sup> Jianlan Wu,<sup>1</sup> Fangchu  
Chen,<sup>2,3</sup> Xuan Luo,<sup>2</sup> Yuping Sun,<sup>2,4,5</sup> Qiunan Xu,<sup>6</sup> Xi Dai,<sup>6,7</sup> and Yi Yin<sup>1,5</sup>

<sup>1</sup>*Department of Physics, Zhejiang University, Hangzhou 310027, China*

<sup>2</sup>*Key Laboratory of Materials Physics, Institute of Solid State Physics,  
Chinese Academy of Sciences, Hefei 230031, China*

<sup>3</sup>*University of Science and Technology of China, Hefei 230026, China*

<sup>4</sup>*High Magnetic Field Laboratory, Chinese Academy of Sciences, Hefei 230031, China*

<sup>5</sup>*Collaborative Innovation Center of Advanced Microstructures, Nanjing 210093, China*

<sup>6</sup>*Beijing National Laboratory for Condensed Matter Physics and Institute of Physics,  
Chinese Academy of Sciences, Beijing 100190, China*

<sup>7</sup>*Department of Physics, Hong Kong University of Science and Technology,  
Clear Water Bay Road, Kowloon, Hong Kong*

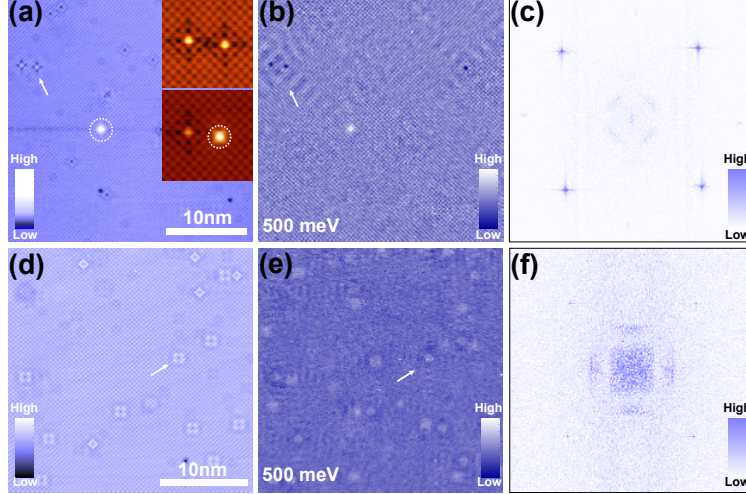


FIG. S1. (a)  $30 \text{ nm} \times 30 \text{ nm}$  topographic image of ZrSiSe ( $V = 500 \text{ mV}$ ,  $I = 400 \text{ pA}$ ). Insets show the process in which an adatom (white dashed circle) is generated from a Zr site defect. Inset images are taken with a junction of  $V = -500 \text{ mV}$ ,  $I = 100 \text{ pA}$ . (b)  $dI/dV$  conductance map at  $500 \text{ meV}$  in the same FOV as (a). (c) Fourier transform of the conductance map in (b). (d)-(f) The same as (a)-(c) but with the data taken at another FOV ( $V = 600 \text{ mV}$ ,  $I = 800 \text{ pA}$ ,  $28 \text{ nm} \times 28 \text{ nm}$ ). White arrows denote the defects which dominate the scattering.

## IMPURITY DEPENDENT QPI PATTERNS

Figure S1(a) and S1(d) are two chosen topographies, mainly with the Zr site defects and Se site defects in the field of view (FOV), respectively. The conductance map simultaneously taken with Fig. S1(a) has dominant standing wave patterns around the cross shaped Zr site defects [Fig. S1(b)]. As shown in Fig. S1(c), the quasiparticle interference (QPI) in this area shows a scattering mainly along the direction of the lattice axes. In contrast, the scattering QPI pattern in Fig. S1(e)-(f) is along a direction with an angle of  $45^\circ$  to lattice axes. The impurity dependent QPI dispersion is also observed in ZrSiS (ref. 21), possibly originating from the different sensitivity of various defects to the band structure.

The cross-shaped Zr site in Fig. S1(a) is different from that in Fig. 1 in the main text. In Fig. S1(a), we also notice an adatom on top of the surface, as denoted by the white dashed circle. As shown in the inset of Fig. S1(a), the lower inset with an adatom is evolved from the upper inset after several images taken in the same FOV. We thus conclude that the adatom is generated from the cross shaped Zr site defect.

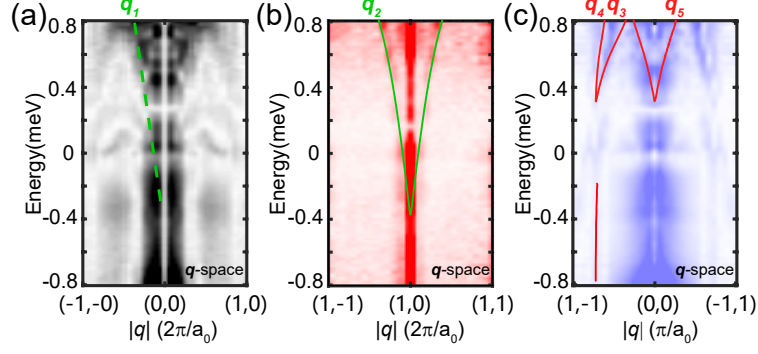


FIG. S2. (a) QPI dispersion along the X- $\Gamma$ -X direction. The  $\mathbf{q}_1$  vector is highlighted by the green dashed line. (b) and (c) QPI dispersion along the M-X-M and M- $\Gamma$ -M directions. DFT calculations of the QPI dispersion are superimposed on the experimental data.

## COMPARISON OF THE QPI DISPERSION BETWEEN THE EXPERIMENT AND DFT CALCULATION

Figure S2(a) presents the experimental QPI dispersion along the X- $\Gamma$ -X direction. The  $\mathbf{q}_1$  vector shows a nearly linear dispersion within the energy range we measured. It also forms a Dirac cone at  $\sim -400$  meV, which is consistent with the dispersion of  $\mathbf{q}_2$  and the relation between  $\Delta\mathbf{q}_2$  and  $\mathbf{q}_1$ . The experimental QPI dispersion along the M-X-M and M- $\Gamma$ -M directions are reproduced from Fig. 4(a) and 4(b), as shown in Fig. S2(b) and S2(c). With the density functional theory (DFT) calculation of the slab band structure and a selection rule discussed in the main text, we further calculate the QPI dispersion along these high-symmetry directions. The calculated QPI dispersion is superimposed on its experimental data, as shown in Fig. S2(b) and S2(c). A quantitative consistence between the experiment and the DFT calculation further verify our analysis of the scattering wavevectors in the main text.

## FULL ENERGY RANGE OF THE QPI PATTERNS

The full evolution of the QPI patterns about the single defect in the inset of Fig. 3(a) is available in Movie S1.